



Towards the Virtual Rheometer: High Performance Computing for the Red Blood Cell Microstructure

Athena Economides
Computational Science and
Engineering Laboratory
ETH Zürich
Clausiusstrasse 33
Zürich CH-8092, Switzerland

Dmitry Alexeev
Computational Science and
Engineering Laboratory
ETH Zürich
Clausiusstrasse 33
Zürich CH-8092, Switzerland

Diego Rossinelli
Lucid Concepts AG
Technoparkstrasse 1
Zürich CH-8005, Switzerland

Lucas Amoudruz
Computational Science and
Engineering Laboratory
ETH Zürich
Clausiusstrasse 33
Zürich CH-8092, Switzerland

Sara Nizzero^{*}
Dept. of Nanomedicine
Houston Methodist Research Inst.,
TX 77030, USA

Sergey Litvinov
Computational Science and
Engineering Laboratory
ETH Zürich
Clausiusstrasse 33
Zürich CH-8092, Switzerland

Panagiotis E. Hadjidoukas
Computational Science and
Engineering Laboratory
ETH Zürich
Clausiusstrasse 33
Zürich CH-8092, Switzerland

Petros Koumoutsakos^{†‡§}
Computational Science and
Engineering Laboratory
ETH Zürich
Clausiusstrasse 33
Zürich CH-8092, Switzerland

ABSTRACT

Recent advances in medical research and bio-engineering have led to the development of devices capable of handling fluids and biological matter at the microscale. The operating conditions of medical devices are constrained to ensure that characteristic properties of blood flow, such as mechanical properties and local hemodynamics, are not altered during operation. These properties are a consequence of the red blood cell (RBC) microstructure, which changes dynamically according to the device geometry. The understanding of the mechanics and dynamics that govern the interactions between the RBCs is crucial for the quantitative characterization of blood flow, a stepping stone towards the design of medical devices specialized to the patient, in the context of personalized medicine. This can be achieved by analyzing the microstructural characteristics of the RBCs and study their dynamics. In this work we focus on the quantification of the microstructure of high and low hematocrit

blood flows, in wall bounded geometries. We present distributions of the RBCs according to selected deformation criteria and dynamic characteristics, and elaborate on mechanisms that control their collective behavior, focusing on the interplay between cells and shear induced effects.

CCS CONCEPTS

- Applied computing → Life and medical sciences; Physical sciences and engineering;

KEYWORDS

Microfluidics, Microstructure, Red Blood Cells, Wall bounded geometries, Taylor-Couette flow, Dissipative Particle Dynamics, High Performance Computing

ACM Reference format:

Athena Economides, Lucas Amoudruz, Sergey Litvinov, Dmitry Alexeev, Sara Nizzero, Panagiotis E. Hadjidoukas, Diego Rossinelli, and Petros Koumoutsakos. 2017. Towards the Virtual Rheometer: High Performance Computing for the Red Blood Cell Microstructure. In *Proceedings of PASC '17, Lugano, Switzerland, June 26–28, 2017*, 13 pages.
<https://doi.org/10.1145/3093172.3093226>

^{*}Also with Applied Physics Graduate Program, Rice University, Houston, TX 77005, USA.

[†]Corresponding Author: petros@ethz.ch

[‡]Also with Radcliffe Institute of Advanced Study, Harvard University, MA, USA.

[§]Also with Massachusetts Institute of Technology, MA, USA.

Permission to make digital or hard copies of all or part of this work for personal or classroom use is granted without fee provided that copies are not made or distributed for profit or commercial advantage and that copies bear this notice and the full citation on the first page. Copyrights for components of this work owned by others than the author(s) must be honored. Abstracting with credit is permitted. To copy otherwise, or republish, to post on servers or to redistribute to lists, requires prior specific permission and/or a fee. Request permissions from permissions@acm.org.

PASC '17, June 26–28, 2017, Lugano, Switzerland

© 2017 Copyright held by the owner/author(s). Publication rights licensed to Association for Computing Machinery.

ACM ISBN 978-1-4503-5062-4/17/06...\$15.00
<https://doi.org/10.1145/3093172.3093226>

1 INTRODUCTION

Blood transport is a central process of the human body functionality and has been the point of interest of numerous clinically relevant studies. It is now well-established that the transport properties and rheology of blood are mainly governed by the mechanical interactions between red blood cells (RBCs), as well as hydrodynamic interactions with the surrounding plasma [14].

The morphology, deformability and mechanics of erythrocytes have a fundamental role in the development of certain hereditary diseases. For example, the severity of hereditary spherocytosis (HS) and hereditary elliptocytosis (HE), increase with mutations of the spectrin connectivity network that holds the skeleton together [7, 17, 75]. This results in mechanical instability of the RBC membrane, that leads to higher deformation, fragmentation and surface and volume loss. Sickle cell disease (SCD) is another example of a disease originating from a change in the RBC microstructure. The erythrocytes exhibit stiffer membrane and higher intracellular viscosity, which results into an impaired flow through microvessels [34, 35]. Another example can be found in malaria, where RBCs infected by *P. falciparum* parasite are again stiffer, lose their biconcave shape, and acquire cytoadherence properties [30, 31, 55]. In all these examples, the microstructural origin of the disease enables a new concept of microrheology-based differentiation and diagnostic tools.

Despite remarkable advances in the field of hemorheology, experiments have limitations in the type and detail of information they can provide regarding the microstructure. The acquisition of information for blood microrheology, including complex phenomena occurring at the microscale, such as cell merging, lysis [58] and biochemical signaling [39, 40, 81], remains a compelling task [59]. Simulations capable of handling such complex dynamical systems at the microscale, are becoming an invaluable tool in complementing the experiments. The modeling and simulation of these systems posses a formidable technological challenge, as they must correctly capture the strong non-Newtonian flow properties, hydrodynamic interactions between different cells, and possible variations in the cell concentration throughout the domain.

In the field of hemorheology, the consideration of microrheological properties has direct practical applications towards the establishment of links with macroscopic quantities, allowing for predictions of blood flow in the majority of vessels and medical devices. A number of research groups [9, 14, 69] reported the first theories regarding the correlation of the RBC microstructure and macroscopically observed quantities, such as the viscosity. These studies were strengthened by the invention of the GDM viscometer[29], that enabled accurate computation of the blood viscosity, through shear stress measurements at low shear rates (0.1 sec^{-1}) [54]. Since then, the rotational viscometer is one of the most widely used rheometers for blood viscosity estimation.

The shear-thinning behavior of blood viscosity has been attributed to the rotation of the RBC membrane, accompanied by a circulation of the enclosed hemoglobin, similarly to the established theory for deformable drops in shear flow [69]. The rotation of the inner fluid induces a transmission of shear stresses towards the contents of the membrane, allowing them to participate in the flow [77]. This effectively leads to the experimentally observed decrease in viscosity with increasing shear rates [14]. However, these theories were derived by connecting typical RBC behaviors in different shear rates to the viscosity change. Through simulations of individual RBCs, we can provide a detailed characterization of the suspended blood cells and directly connect the viscosity to specific RBC motion and conformation. The rich dynamics of a single RBC were exploited more during the last decades, leading to the

identification of three shear rate regimes, with distinct RBC behaviors: tumbling, swinging and tank-treading [1, 72]. However, it has been recently shown that this behavior changes significantly when higher RBC concentrations are considered [47]. In this case, the RBCs can assume a variety of shapes and orientations, all of which have an implication on the overall viscosity of the suspension.

Advancements in the field of computational science and engineering have led to the development of software with the potential to contribute to experimental findings. The effective integration of mathematical models with data, under the uncertainty quantification framework, has lead to reliable calibration of model parameters [78]. The calibration of complex and computationally demanding physical models is becoming possible, through software that are able to exploit the capabilities of massively parallel and hybrid (CPU/GPU) computer architectures [33]. Currently, the majority of simulations used for microfluidic systems are based on continuum models. Solvers of grid based and Boundary Integral methods have exhibited excellent scalability [66], and are used for the solution of the linear viscous Stokes equations, with the capability of handling the complex geometries of microfluidic devices. However, such solvers have limited capabilities in resolving essential sub-micron flow biophysics [26] and the neglect of transport properties at the microscale may lead to the overlooking of important effects [56]. In addition, state-of-the-art boundary integral simulations of RBCs, have only used a few hundred RBCs in two-dimensional geometries [26, 64] and lower resolution models are considered [42]. Mesoscale models, such as Lattice Boltzmann (LB) [13] use discrete particles to represent flows in microfluidic channels. However, the LB kernel is memory intensive and hardly achieves a significant percentage of peak performance in modern computing architectures [8, 68]. Additionally, as the Reynolds number approaches zero, the accuracy of the method decreases and the computational cost increases, thus limiting the applicability to microfluidics [26]. On the other hand, the computational cost of employing Molecular Dynamics (MD) simulations for high concentration blood flows in microscopic scales is currently prohibitively high. MD simulations were coupled to Dissipative Particle Dynamics (DPD) in a two-step multiscale framework, to accurately capture the mechanical properties of RBCs [12], showing distinct membrane behaviors of healthy and defective RBCs under stretching.

Our simulations are based on an extension of the Dissipative Particle Dynamics (DPD) method, originally proposed by Hoogerbrugge and Koelman [38], a particle-based stochastic mesoscopic method that bridges the gap between MD and the Navier-Stokes equations [32]. DPD has been extensively used for the modeling of complex systems [5, 51] and has become a key method for the study of blood microrheology [48, 80] and blood microfluidics for cancer therapy [45, 57]. State of the art DPD solvers are based on extensions of software packages originally developed for MD simulations, such as LAMMPS [63] and HOOMD-Blue [4], with the capability of running on both CPU-only and GPU-accelerated supercomputers. For our simulations, we use *uDeviceX*, a high-throughput open source package with kernels thoroughly optimized for GPUs, for microfluidic simulations using state-of-the-art DPD models [68].

In this paper, we simulate the flow of RBCs inside a two concentric cylinders setup, with the aim to approach the behavior of blood

in devices such as the GDM viscometer. We observe the microstructural characteristics of the RBCs by focusing on their shape and deformation, with respect to their position inside the device. These observations are based on distributions of bending energy, radius of gyration, asphericity, acylindricity, relative shape anisotropy and orientation. Our results are the outcome of collaborative and interdisciplinary research, bridging scientific fields concerned about complex fluid rheology, bioengineering and computational science. To our knowledge, these are the first results that present information related to the microstructure of RBCs in a viscometric device, obtained from three dimensional simulations of individual RBCs. Previous related works studied the effects of vesicle suspensions on mixing [41, 42], in two dimensional Taylor-Couette flows in the zero Reynolds number regime. In addition, [28] performed two dimensional simulations of vesicles in Taylor-Couette flow, using the boundary integral method, focusing on vesicle migration and flow disturbance at the presence of a single and multiple vesicles. We wish to contribute to the efforts towards the accurate modeling of blood microfluidics and provide insights to the dynamics of the microstructural arrangement of the blood constituents, and its implications to the observed micro- and macro-rheology.

This paper is structured as follows: Section 2 provides details for the mathematical model and the boundary conditions between the different combinations of particle interactions. In Section 3, we present the software that is used in our simulations, along with details on its performance. In Section 4, we specify the simulation setup and perform the necessary validation tests by comparing the output of our DPD simulations to results obtained from simulations using the Boundary Element method. Section 5 presents the results of high and low hematocrit simulations inside a Taylor-Couette setup, focusing on macro- and micro-scopic flow properties and characteristics. Our findings are summarized and further discussed in Section 6. Additional information regarding the simulation setup and parameters is included in the Appendix.

2 NUMERICAL METHODS

2.1 Dissipative particle dynamics

Following recent works [24, 36, 68], we model blood as a suspension of RBCs using Dissipative Particle Dynamics. DPD is a mesoscopic method which assumes a coarse grained representation of the system: the number of degrees of freedom is reduced by representing clusters of molecules with soft particles, to simulate fluids on a mesoscopic scale [23]. Essentially it is an N-body algorithm where discrete particles interact through pairwise forces. We denote by $\mathbf{r}_{ij} = \mathbf{r}_i - \mathbf{r}_j$ the vector between particle centers i and j , and by $\mathbf{v}_{ij} = \mathbf{v}_i - \mathbf{v}_j$ their relative velocity. The particle's position and velocity are updated through Newton's second law: $m_i \frac{d\mathbf{v}_i}{dt} = \mathbf{f}_i$, where \mathbf{f}_i is the total force applied on particle i . It is computed as a sum of three forces each of which is pairwise additive [32].

$$\mathbf{f}_i = \sum_{i \neq j} \left(F_{ij}^C + F_{ij}^D + F_{ij}^R \right) \hat{\mathbf{r}}_{ij}$$

The conservative force, F_{ij}^C , is a soft repulsion between two particles. The dissipative force, F_{ij}^D , represents the energy loss caused by

frictional effects. The random force, F_{ij}^R , represents the energy increase by including the effect of the suppressed degrees of freedom in the form of thermal fluctuations.

$$\begin{aligned} F_{ij}^C &= a w^C(r_{ij}) \\ F_{ij}^D &= -\gamma w^D(r_{ij}) (\hat{\mathbf{r}}_{ij} \cdot \mathbf{v}_{ij}) \\ F_{ij}^R &= \sigma w^R(r_{ij}) \zeta_{ij} \Delta t^{-1/2} \end{aligned}$$

w^D , w^R , and w^C are weight functions that are zero for $r > r_c = 1$, where r_c is the cutoff radius, and ζ_{ij} is a Gaussian random variable with zero mean and unit variance that is drawn independently for each pair and timestep.

In this work we choose the following weight functions:

$$\begin{aligned} w^C(r_{ij}) &= 1 - r_{ij} \\ w^D(r_{ij}) &= (w^R(r_{ij}))^2 = (1 - r_{ij})^k \end{aligned}$$

where k is an envelop parameter. The connection between random and dissipative forces is set by the fluctuation-dissipation theorem [18].

$$\sigma = \sqrt{2\gamma k_B T}$$

where k_B is the Boltzmann constant and T is the temperature in absolute units.

2.2 RBC model

The RBC membrane is represented by DPD particles composing the vertices of a two-dimensional triangulated network forming the RBC surface [23]. Incident mesh triangles have an associated potential energy depending on the angle between them, and local and global area constraints are enforced, along with a global volume constraint.

The total potential energy of the system is [22]

$$U = U_{\text{in-plane}} + U_{\text{bending}} + U_{\text{area}} + U_{\text{volume}}$$

$U_{\text{in-plane}}$ accounts for the energy of the elastic spectrin network of the RBC membrane, including an attractive wormlike chain potential and a repulsive potential such that a nonzero equilibrium spring length can be obtained

$$U_{\text{in-plane}} = \sum_{j \in 1 \dots N_s} \left[\frac{k_B T l_m (3x_j^2 - 2x_j^3)}{4p(1 - x_j)} + \frac{k_p}{l_0} \right]$$

where x_j is the normalized spring length and N_s is the number of springs.

The bending energy term, U_{bending} , models the bending resistance of the lipid bilayer and is equal to

$$U_{\text{bending}} = \sum_{j \in 1 \dots N_s} k_b [1 - \cos(\theta_j - \theta_0)] \quad (1)$$

where k_b is a bending constant and θ_j is the angle between two adjacent mesh triangles.

U_{area} and U_{volume} represent the area and volume conservation constraints, which mimic the area-incompressibility of the lipid bilayer and the incompressibility of the inner cytosol, respectively.

$$U_{\text{area}} = \frac{k_a (A^{\text{tot}} - A_0^{\text{tot}})^2}{2A_0^{\text{tot}}} + \sum_{j \in 1 \dots N_t} \frac{k_d (A_j - A_0)^2}{2A_0},$$

$$U_{\text{volume}} = \frac{k_v(V - V_0^{\text{tot}})^2}{2V_0^{\text{tot}}}, \quad A^{\text{tot}} = \sum_{j \in 1 \dots N_t} A_j$$

where A_j is the area of one triangle, V is the volume enclosed by the membrane and N_t is the number of triangles used for the discretization of the RBC membrane.

The mass of the membrane particles is adjusted through a separate study of a single cell in a Taylor-Couette flow, by comparing to results obtained with the Boundary Element Method. We find that for the solvent viscosity and angular velocity used, the mass of the RBC particles should be half the mass of the solvent particles, $m_m = 0.5m_s$ such that inertia effects are balanced by pressure. For tumbling cells, no significant radial migration is observed, a result confirmed by [28]. The values of the membrane model parameters are given in the Appendix. In this study we use the same DPD parameter values that were used in [24], for solvent viscosity of $\eta_0 = 26.3$ (see Appendix, Table S2 in [24]), with rescaled length-dependent parameters such that $r_c = 1$ in DPD units.

In the RBC model, the values of k_a, k_d, k_v are taken from [21]. We use the RBC mesh consisting of $N_v = 498$ vertices, based on the coarse-graining convergence studies presented in [21] and [62]. The membrane triangulation follows [21] and the number of triangles is related to the number of vertices as $N_t = 2N_v - 4$. From the outcome of ongoing uncertainty quantification studies for the current RBC model conducted within our group, we choose the values of A_0^{tot}, l_0 and p shown in Table 2. The procedure and values used to compute the model $k_B T$ and θ_0 , are described in [21] and [24].

2.3 Wall-RBC and RBC-RBC interactions

Solid walls are modeled using “frozen” particles – particles which have a prescribed wall velocity and are not subjected to position update. Following the work and terminology of [25] we use the *EBC-0* boundary condition, which considers a pre-processing stage with a DPD fluid at equilibrium and periodic boundary conditions, and subsequent freezing of the positions of the DPD particles that occupy the regions of solid walls after system equilibration. This boundary condition and its performance in terms of no-slip enforcement and density oscillations is described in detail in [25]. Due to the soft DPD interactions, fluid particles are not fully prevented from penetrating the wall. Therefore, we use a bounce-back boundary condition for both the solvent and solute particles, which re-inserts any crossing particles into the fluid domain, with opposite velocity [67].

The interactions between different RBCs are modeled through a short-ranged purely repulsive Lennard-Jones potential in addition to the DPD force field, in order to ensure that there is no overlapping between RBCs.

$$U_{\text{LJ}} = 4\epsilon_{\text{LJ}} \left[\left(\frac{\sigma_{\text{LJ}}}{r} \right)^{12} - \left(\frac{\sigma_{\text{LJ}}}{r} \right)^6 \right]$$

The values of σ_{LJ} and ϵ_{LJ} are taken from [24]. ϵ_{LJ} is rescaled as described in the previous subsection.

The RBC-solvent interactions are modeled through the DPD forces. The DPD parameter values used are chosen from Table S1 in [24], and correspond to solvent viscosity $\eta = 26.3$ in DPD units.

3 SOFTWARE

We use *uDeviceX* (ACM Gordon Bell Prize Finalist 2015), a high-throughput open-source software (<https://github.com/uDeviceX/uDeviceX>) with kernels thoroughly optimized for GPUs, aimed at microrheology simulations using state-of-the-art DPD models. *uDeviceX* has been shown to perform unprecedented simulations of blood flow and circulating tumor cells with sub-micron resolution in realistic microfluidic geometries [68].

uDeviceX is targeting GPU-enabled clusters, such as *Titan* at Oak Ridge National Laboratory and *Piz Daint* at CSCS. The parallelization approach of the code can be arranged in the cluster and GPU levels. Cartesian domain decomposition is employed on the cluster level, with asynchronous MPI communications overlapped dominantly with the computational kernels. GPU level parallelism is exposed through per-particle SIMD kernels, detailed description of which is available in [68].

uDeviceX is reported to outperform LAMMPS [63] by a factor of up to 45 times and HOOMD-Blue by a factor of 3 – 4 times. Moreover, *uDeviceX* reaches up to 65.5% of the nominal aggregate CPU+GPU peak performance in terms of Executed Instructions Per Cycle (IPC) for the most computationally-intensive kernel and 34% overall. Finally, it achieves an excellent weak efficiency of more than 99% and strong efficiency of 94% on the Piz Daint supercomputer. Representative performance results are depicted in Table 1. *uDeviceX* is capable of handling domains up to 35 mm^3 at sub-micron resolution, containing 385 million deforming RBCs on the Piz Daint supercomputer.

4 SETUP AND PRELIMINARY RUNS

4.1 Simulation setup

We simulate blood flow between two concentric cylinders of radii R_{in} and R_{out} (see Fig 1). The inner cylinder is fixed and the outer cylinder rotates with angular velocity Ω_{out} . The domain is $L_{\text{axial}} = 32$ DPD units in axial direction and 216×216 in the plane perpendicular to the axis. Periodic boundary conditions are applied in the axial direction. The hematocrit values chosen for the simulations, correspond to the average hematocrit for whole blood (45%), and the hematocrit observed in human microvessels (15%) which is lower than the average, as a consequence of the Fahraeus-Lindqvist effect as well as the irregular distribution of RBCs in vessel bifurcations [27, 53]. For this geometry, in the case of the high RBC concentration, we use 10^4 RBCs, and 6.5×10^6 solvent particles (corresponding to number density $n_d = 10$). The simulations are run in single precision on 96 nodes on the Piz Daint supercomputer (Cray XC30, Swiss National Supercomputing Center). In order for the system to reach a steady state, the simulation is run for 10^7 steps, corresponding to $t = 5$ seconds, with a timestep of $\Delta t = 0.0005$ DPD time units.

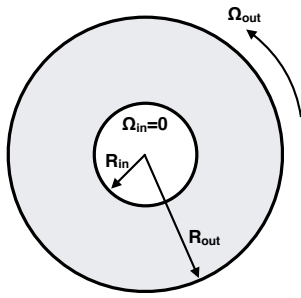
4.2 Verification and validation

The RBC and DPD models have been extensively validated in several previous studies [3, 21, 24, 50]. In [50] the DPD model is validated with respect to experimental data from [79], theoretical studies by [10] and [16], analytical solutions [60, 73] and continuum Navier-Stokes solvers from [44] and [2]. In [3] the DPD model

Table 1: Measured strong scaling (left) and weak scaling efficiency (%) over 1 node (right) on Piz Daint.

Nodes	Speedup	Efficiency
625	-	-
1250	1.98	98.9%
2500	3.82	95.4%
5000	7.50	93.8%

Ranks / node	Nodes				
	1	625	1250	2500	5000
1	-	98.3	98.2	98.2	97.7
2	-	99.7	99.4	99.1	98.6
4	-	99.6	99.7	99.7	99.7
8	-	99.9	99.9	99.9	99.9

**Figure 1: Simulation setup: Taylor-Couette flow with stationary inner cylinder and rotating outer cylinder at constant angular velocity Ω_{out} .**

is validated with respect to analytical solutions and experimental data for flow past a cylinder. The RBC model is verified against single-cell stretching experiments and single-cell flow in stenotic channels in [21, 49, 65]. In [24] the derived blood viscosity from multiscale simulations of interacting RBCs is verified with respect to the experimental shear viscosity of well-prepared nonaggregating erythrocyte suspensions (ES) and to the shear viscosity of whole blood.

4.2.1 Comparison to analytical solution. To draw conclusions regarding the effect of the presence of the RBCs on the flow, we first run a case where only solvent is considered (i.e. no RBCs are present). We map the obtained particle data to continuum space by dividing the simulation domain into bins and averaging over each bin and over time. In Fig. 2, the velocity is compared with the analytical solution of the Taylor-Couette flow [46]:

$$v(r) = \frac{\Omega_{\text{out}} R_{\text{out}}^2}{R_{\text{out}}^2 - R_{\text{in}}^2} \left(\frac{R_{\text{in}}^2}{r} - r \right) \quad (2)$$

Note that the shear stress in this flow is proportional to $1/r^2$ and the ratio between stresses on inner and outer cylinders is $R_{\text{out}}^2/R_{\text{in}}^2 \approx 7$.

The particle density distribution is shown in Fig. 2(A). The results indicate that the flow and the boundary conditions at the wall do not introduce further perturbations in the fluid density of the DPD simulation. In addition, the velocity profile is found to be in good agreement with the theoretical predictions (Fig. 2(B)). We note that the data shown in Fig. 2(A,B) are cell-centered quantities along the radial direction, where the first and last cells are adjacent to the prescribed wall location.

4.2.2 Comparison to boundary element method. We use the Boundary Element Method (BEM) with regularized kernels as described in [15], to simulate the trajectory of a single solid RBC in a Taylor-Couette flow, at the limit of zero Reynolds number (Stokes flow). We compare the results of the BEM solution to the DPD simulation of the flow of one RBC inside a Taylor-Couette flow. The comparison is shown in Fig. 2(C,D). The position of the center of mass of the RBC during an entire cycle of the RBC inside the domain is plotted in Fig. 2(D). We observe that the DPD results show an excellent agreement with the reference BEM results. Our results are in agreement with [28] showing no migration in the case of a tumbling cell. The orientation angle of the RBC at the plane of shear with respect to the distance traveled by the RBC's center of mass (COM), is presented in Fig. 2(C). The DPD results comply well with the BEM results. The light flickering in the DPD data is caused by the random thermal fluctuations of the RBC membrane.

5 RESULTS

5.1 Macroscopic flow properties

To observe the effect that the RBCs have when immersed in a Newtonian solution, we simulate RBCs flowing inside a Taylor-Couette setup. We perform two simulations with different volume fraction of RBCs (hematocrit): $Ht = 15\%$ and $Ht = 45\%$. While our approach can be applied to much lower or higher hematocrit regimes, we here show results from two values that represent the most clinically relevant values of *in vivo* human systemic hematocrit (45%) [19], and human microcapillary hematocrit (15%) [11]. Furthermore, values of 15% hematocrit are often used in microfluidic devices [43].

Figs. 3(A,D) show the average particle density along the radial direction. The total density of the system (black line) is uniform in the interior of the domain and presents small oscillations on the edges, as a result of the space confinement, due to the presence of the cylindrical walls. The jump in the density profile near the walls is expected, as the boundary conditions used for the wall determine the presence of near-wall oscillations in density, and several previous studies have addressed this issue [3, 25, 61, 74]. Details about the boundary conditions that we use can be found in Section 2. By comparing the density profile for the DPD (blue line) and the RBC (red line) particles, we observe an increase in the solvent density and a decrease in the RBC density near the wall. This demonstrates that the cells migrate away from the wall, creating a “cell-free” layer (CellFL). The CellFL has been observed in *in-vitro* experiments of blood flow through microvessels [23] and is the origin of the Fahraeus-Lindqvist effect [20].

Figs. 3(B,E) depict the normalized momentum distributions in the system. By focusing on the total momentum (black line), we

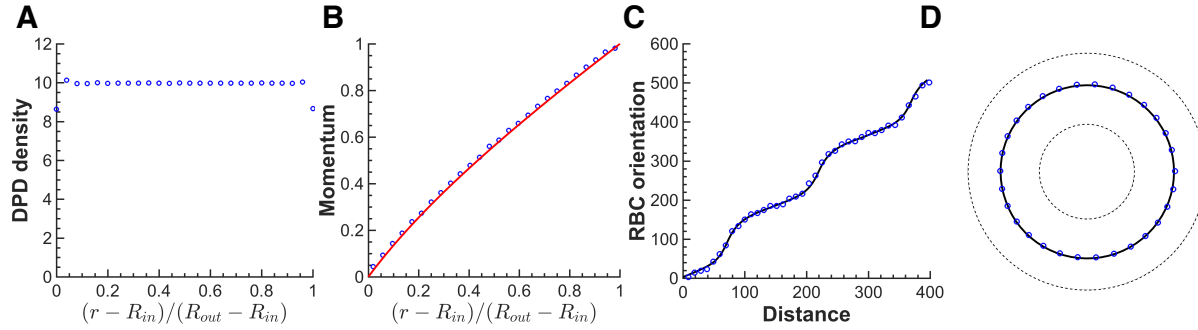


Figure 2: Comparison to Analytical and BEM solutions: Blue: DPD simulation results. Red: Analytical solution for Newtonian fluid. Black: BEM simulation results. (A) DPD particle number density along radial direction. (B) Normalized momentum in the azimuthal direction along the radial direction. (C) Orientation of the cell with respect to the distance covered by the center of mass. (D) Single RBC simulation: Trajectory of the center of mass of the cell. Dotted lines represent the wall boundaries.

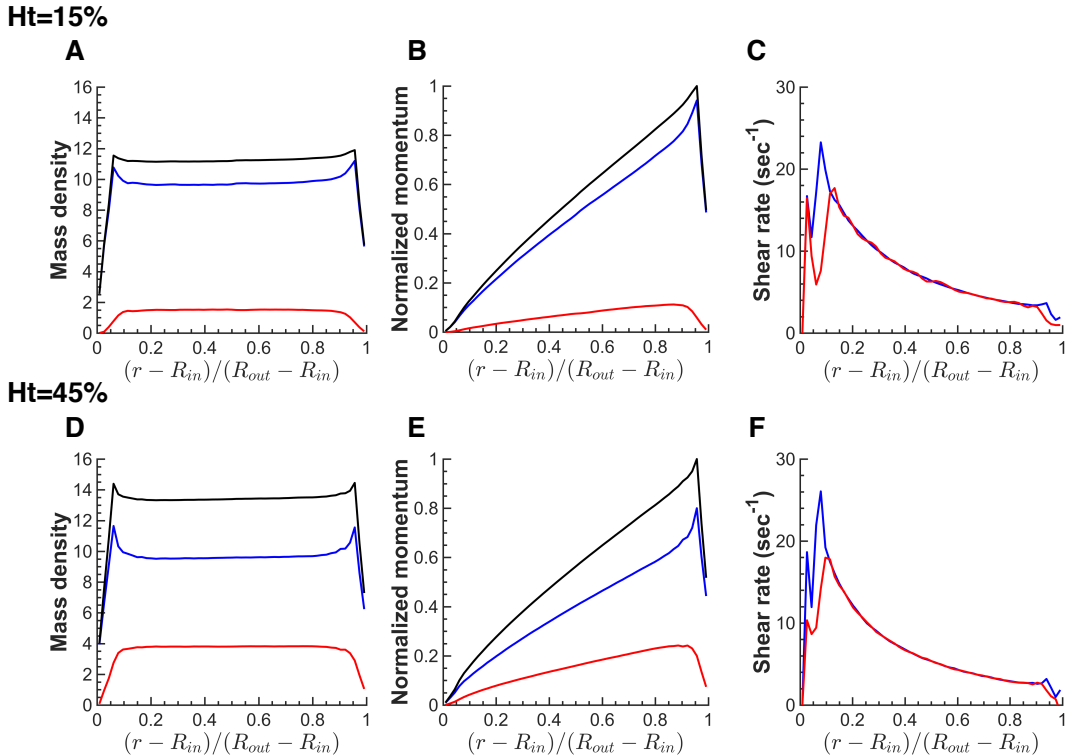


Figure 3: Blue: Solvent quantities. **Red:** RBC quantities. **Black:** mass weighted averaged solvent and RBCs quantities. (A,D) Mass density along the radial direction. (B,E) Normalized azimuthal momentum. (C,F) Shear rate obtained by numerical differentiation of the average particle velocity, converted to physical units (SI).

observe that the presence of the RBC particles lead to a significant change in the qualitative behavior of the total momentum distribution, originating from deviations of the overall density with respect

to the only-solvent case (see Fig.4). Figs. 3(B,E) both have a peak for momentum, a feature that is not present in the momentum profile of the pure solvent 2(B). This reveals the highly non-Newtonian

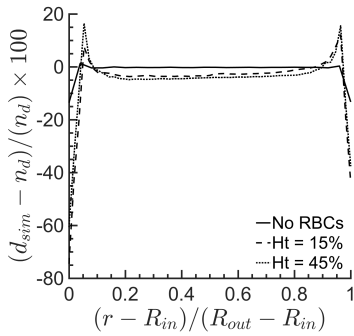


Figure 4: Comparison of density profiles between the results of pure solvent and results where cells are present.

behavior of blood. We believe that this difference is a direct consequence of the CellFL, which causes a redistribution of the RBCs inside the domain, leading to regions with high viscosity contrasts. The depletion of near wall regions from RBCs has been also observed in recent Boundary Integral simulations of vesicles in a Taylor-Couette flow [42] in 20% and 40% volume fractions.

In the region of the CellFL the total momentum has a higher but finite slope. This leads to a locally higher shear rate near the inner wall, where large velocity variations occur, due to the imposition of zero wall velocity. In both simulations the shear rate is changing up to 7 times along the radial direction, from one wall of the domain to the other. The physical range of shear rates covered in our simulations is $3.5 - 27 \text{ sec}^{-1}$ (Fig. 3(C,F)). In this range the viscosity of aggregating and non-aggregating blood is the same [14].

The viscosity of the blood is expected to decrease with increasing shear rate. To interpret the simulated velocity profiles we consider two models: constant viscosity (Newtonian fluid) and Power-law fluid:

$$\eta = \eta_0 \dot{\gamma}^{n-1} \quad (3)$$

The Power-law fluid reduces to the Newtonian fluid for $n = 1$. The analytical solutions were fitted to the simulation data in the region that is not affected by the CellFL. Both models give a good fit for the data, with the Power-law model producing smaller and less regular residuals, especially in the case of $Ht = 45\%$. The parameters of the fit $n = 0.93$ and $n = 0.84$, are recovered for $Ht = 15\%$ and $Ht = 45\%$. This is consistent with the fact that blood is a shear thinning fluid, and non-Newtonian properties are more pronounced for higher concentration of RBCs. The simulated and theoretical velocity profiles are shown in Fig. 5. The difference between the two models is better seen in transformed coordinates by taking the logarithm of the ratio of velocity and distance to wall.

5.2 RBC microstructure characteristics

We now focus on the characterization of the RBCs configuration. By examining visually the slices of the simulation domain in time (see Fig. 6) the following qualitative observations can be made:

- We do not observe a large variety of cell shapes and orientations, as reported recently [47], possibly due to the

relatively low shear rate used in our simulations. Deviations from bi-concave shape are seen only for $Ht = 15\%$ and close to the inner cylinder (the region of higher shear rate).

- There are no clusters or layers of RBCs as postulated by some authors [70, 71].
- Shear stress deforms and orients cells for both concentration, but very few tumbling and tank-treading events are seen.
- Trajectories and conformations of the cells are not qualitatively different between the two concentrations.
- Trajectories and conformations of the cells are not qualitatively different in the bulk and the CellFL.

5.2.1 Microstructural statistics. We now proceed to a quantitative analysis of the cell dynamics and configurations. The results are summarized in Figs. 7 and 8. Fig. 7 presents distributions of six metrics that characterize the configuration and state of the RBCs: bending energy, radius of gyration, asphericity, acylindricity, relative shape anisotropy and orientation angle. This figure is created by using data from the last 20% of the simulation snapshots. This corresponds to approximately 500 data-files, out of which every 10^{th} is used for the construction of the plots in Fig. 7. The membrane bending energy, is computed from Eq. 1. The radius of gyration, R_g is computed as $R_g^2 = \lambda_x + \lambda_y + \lambda_z$, where, $\lambda_x \leq \lambda_y \leq \lambda_z$ are the principal moments of the gyration tensor [52]. The asphericity is computed as $b = \lambda_z - 0.5(\lambda_x + \lambda_y)$ and is always non-negative, and has zero value for a spherical object ($\lambda_x = \lambda_y = \lambda_z$). We compute the acylindricity as $c = \lambda_y - \lambda_x$. The relative shape anisotropy, κ^2 , is computed through a combination of the asphericity and acylindricity, $\kappa^2 = (b^2 + (3/4)c^2) / R_g^4$, and obtains values between 0 and 1, corresponding to spherically symmetric shapes and points in a line, respectively. Finally, the orientation angle is defined as the angle of the cell's principal axis in the azimuthal direction, with respect to the plane of shear (θz -plane).

The bending energy of the RBC membrane is a metric of the deformation that the membrane is subject to, compared to the equilibrium state (see Eq. 1). Different bending regimes correspond to different RBC shapes. Figures 7(A,G) show the distribution of the cells' bending energy along the radial direction. In the case of $Ht = 45\%$, it is observed that the bending energy has a wider distribution near the inner cylindrical wall (Fig. 7(G)). The distribution becomes narrower as the outer wall is approached. This suggests that the RBCs are undergoing larger deformations in the proximity of the inner wall. For the $Ht = 15\%$ (Fig. 7(A)), the bending energy distribution does not have large variances along the radial direction, suggesting that the RBCs are less deformed and retain their original shape.

The radius of gyration, asphericity, acylindricity and relative shape anisotropy, are all related to cell shape characteristics. The radius of gyration relates to the size of the cells, while the rest are scale invariant metrics that contain information related to the configuration of the particles on the cell membrane. By observing the distribution plots of these four metrics, it is seen that the acylindricity has the largest divergence from the mean line, especially for $Ht = 45\%$. Moreover, by comparing the plots between $Ht = 15\%$ and $Ht = 45\%$ (Figs. 7(B,H,C,I,D,J,E,K)), it is observed that

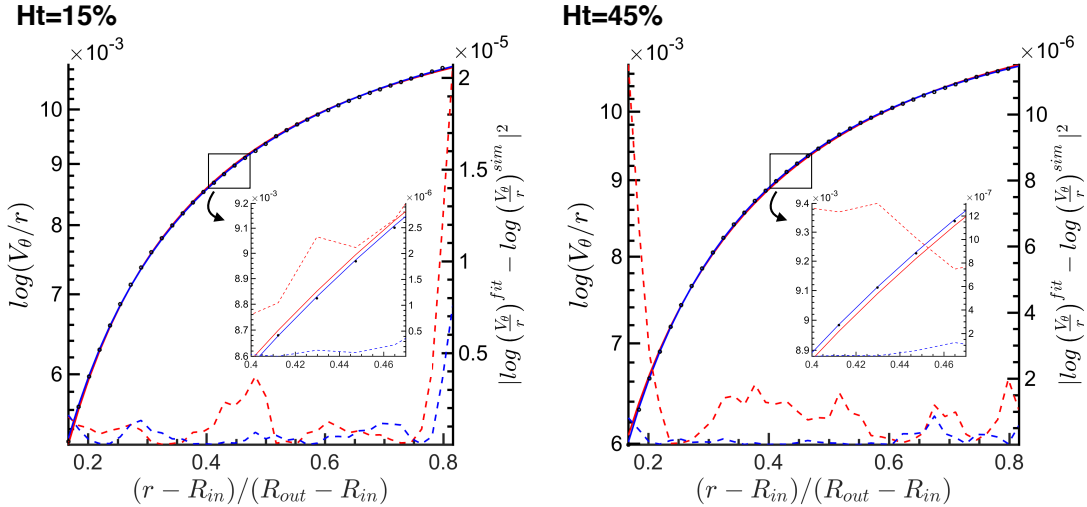


Figure 5: Fit of the azimuthal angular velocity computed as $\log(V_\theta/r)$ along the normalized radial direction. Circles: Simulation results. Solid red line: Newtonian fit. Solid blue line: Power-law fit. Dashed red line: Residuals of Newtonian fit. Dashed blue line: Residuals of Power-law fit.

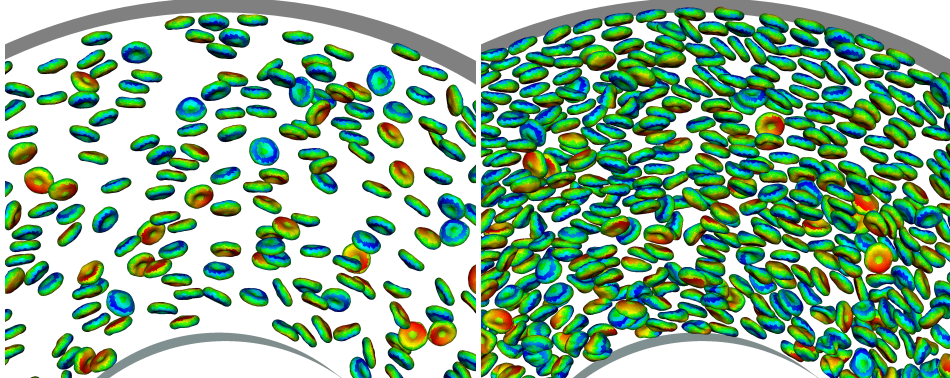


Figure 6: Simulation snapshots in a slice of the domain. The colors on the cells denote the particle-id within the set of particles that compose each cell. The initial configuration (initial particle position on the membrane and cell orientation) is the same for all cells. (Left) $Ht = 15\%$. (Right) $Ht = 45\%$.

the discrepancies from the mean value in the $Ht = 45\%$ case are remarkably larger. The highest divergence occurs in a region closer to the inner wall. This leads to a decrease in the mean value of the radius of gyration, acylindricity and relative shape anisotropy. A closer examination in the relative shape anisotropy at the hematocrit of 45% (Fig. 7(K)), reveals that the cells closer to the inner wall are likely to have a more spherical shape. This is justified by the fact that the relative shape anisotropy is zero for spherically symmetric shapes and is equal to one for linear shapes. For relaxed and isolated RBCs the relative shape anisotropy, κ^2 , has a value of 0.136. At the proximity of the outer wall, the relative shape anisotropy has a value of 0.134, which corresponds to a divergence of only 1.47% from the relaxed value. Closer to the inner wall, the shape anisotropy spans a wide range of values, which suggests that the

cell shape is not uniform anymore but there exists a broader and much more rich collection of cells in terms of shapes.

The eigenvalues of the gyration tensor of the set of DPD particles forming the membrane of the cell, are $\lambda_1^2 \leq \lambda_2^2 \leq \lambda_3^2$. The orientation of the cell is defined as the angle between the eigenvector corresponding to λ_1^2 and the direction from the axis of the cylinders to the cell. The average value of the cells' orientation is plotted with respect to the radial position of the cell's center of mass in Fig. 7(F,L). As shown in the figure, the orientation angle of the cells spans the entire range between 0° and 180° degrees, with average value 90° . It is observed that at the inner wall the orientation angle is lower than the average value in the middle part of the domain. In addition, the standard deviation of the orientation angle along the radial direction is decreased at the points close

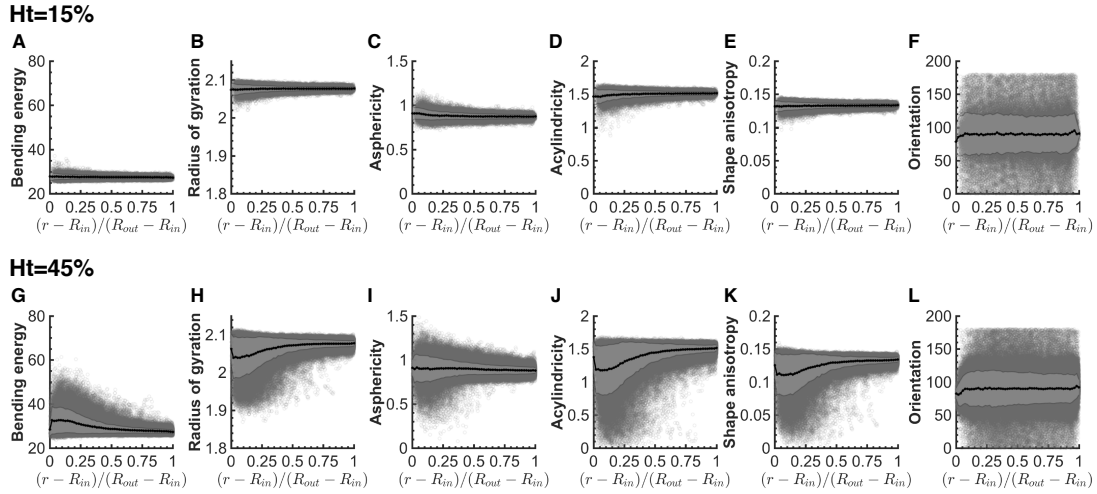


Figure 7: Statistics of the cell's microstructural configuration: Distributions of averaged steady-state quantities along the radial direction, for $Ht = 15\%$ (upper row) and $Ht = 45\%$ (bottom row): (A,G) Bending energy. (B,H) Radius of gyration. (C,I) Asphericity. (D,J) Acylindricity. (E,K) Relative shape anisotropy. (F,L) Orientation angle in degrees. In all plots, the circles correspond to data values, the black line corresponds to the mean value of the observed quantity and the edges of the light gray area, around the mean value, represent the standard deviation.

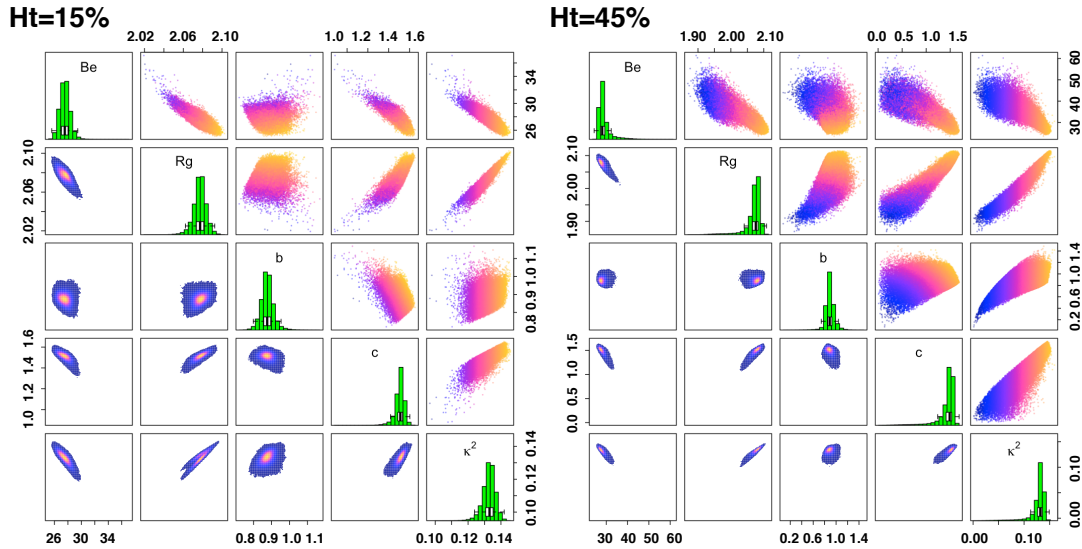


Figure 8: Correlations between the microstructure characterization quantities: Be : Bending energy, Rg : Radius of gyration, b : Asphericity, c : Acylindricity, κ^2 : Relative shape anisotropy. Diagonal: marginal distribution of the quantities of interest, estimated using kernel histograms accompanied by a Tukey boxplot. Above the diagonal: projection of the data values of all pairs in 2D parameter space. Below the diagonal: projected densities in 2D parameter space. (Left) $Ht = 15\%$. (Right) $Ht = 45\%$.

to the inner and outer walls. This implies that the cells flowing near the wall boundaries have fewer deviations in their orientation angle and hence are more uniformly orientated. There is therefore a consensus in the orientation angle of the RBCs that are near the device's walls. The result presented in this section are a first step

towards the construction of a model to predict the RBC shape and deformation distributions, with respect to the hematocrit. However, in order for such a model to be constructed, further studies for additional hematocrit values must be performed.

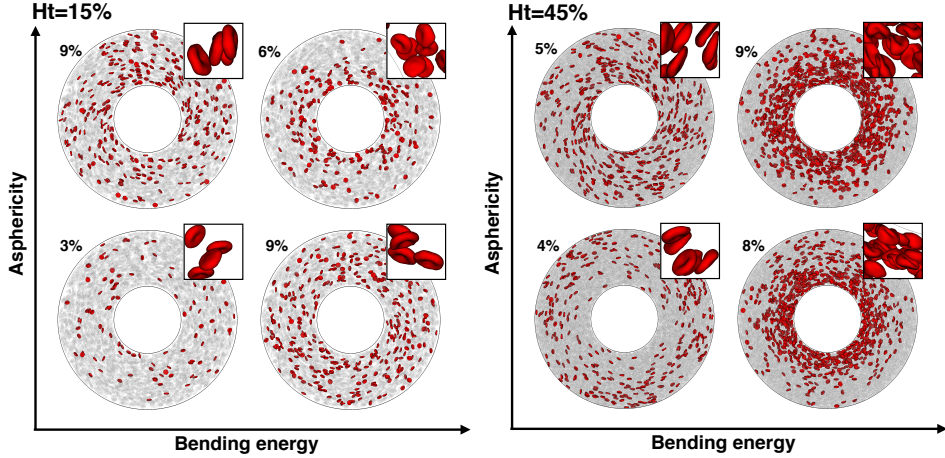


Figure 9: Categorization of cells with respect to their membrane bending energy and asphericity values. The red highlighted cells belong to the first and fourth quantiles of the bending energy and asphericity distributions. (Left) $Ht = 15\%$. (Right) $Ht = 45\%$. The percentages shown in each plot correspond to the fraction of the highlighted cells with respect to the total number of cells.

5.2.2 Microstructural correlations. In order to quantitatively describe the status of the cells, we search for correlations between the deformation of the cells (bending energy) and the cells' shape (gyration radius, asphericity, acylindricity, relative shape anisotropy). Our findings are summarized in Fig. 8. The upper diagonal part of the figures presents the distribution of each quantity, with respect to all other quantities. We focus on the first line of the table, where the bending energy is plotted against the shape characterization metrics. In both hematocrit cases, the bending energy is correlated to the gyration radius, the acylindricity and the relative shape anisotropy. The correlation is more pronounced in the case of $Ht = 15\%$. On the other hand the asphericity has a weaker correlation to the bending energy. In the $Ht = 45\%$ case, a weak trend is observed which relates increases to the asphericity to decreases in the bending energy. However, for each bending energy, a cell could acquire any value within a broad range of asphericity values. Therefore, in order to gain more information regarding the state of the cells we proceed to a classification according to the bending energy and asphericity values.

In order to see how asphericity and bending energy affect the cell shape we create a qualitative matrix plot with snapshots of instantaneous RBC shapes and configurations (Fig. 9). Each quarter of the plot highlights with red the cells that belong in the specified asphericity-bending energy region. In the $Ht = 15\%$ case, there are no large deviations of the cell shape from the unstrained one. This observation is confirmed by Fig. 7(A) where it is clearly shown that the deviations from the mean value of the bending energy are negligible in comparison to the deviations in the case of highly concentrated cells. In contrary, at $Ht = 45\%$ (Fig. 9, right plot), one can clearly see that at high membrane bending energies, the cell shape is considerably different from the original one. In this regime, low asphericity cells seem to have a spherical-like shape, which complies with low asphericity values. In the case of high bending energy and high asphericity, the cells' shape can no longer

be uniformly characterized, as the cells in this region are exposed in high deformations, with twists and peaks in the membrane leading to highly irregular shapes. In the low bending energy regime, we observe that in general the membrane retains its smoothness without having any peaks. More specifically, at low bending energy and low asphericity, the disk-like shape of the cells resemble the original RBC biconcave shape closely. At low bending energy and high asphericity values the cells are stretched, especially in the region near the inner cylindrical wall. By connecting the results of Fig. 3(F) to the results presented in Fig. 9 for $Ht = 45\%$, we conclude that high shear rates result to cells with high bending energy. Furthermore, in the cases considered, the shear rate does not influence the asphericity.

6 CONCLUSIONS

In the past decades, several experimental studies have investigated the importance of RBC shape changes on its biological functionality [6, 37, 76] and their relationship to certain blood diseases. Our work provides the computational approach to microrheology-based diagnostic tools.

We perform simulations of the “virtual rheometer” for blood: a Taylor-Couette flow with solid walls. The density, velocity and shear rate profiles are reported separately for RBCs and for plasma. By fitting the average velocity profile, we find that the Power-law model offers a good fit for the velocity profile for low and high concentration of RBCs. Regarding the dynamics of the RBCs, we observe that the majority of the cells are not involved in tumbling and tank-treading motion. Moreover, no high level structures (layers or clusters) are found.

In addition, we provide insights into the microstructure by quantitatively describing the state of the cells using metrics that relate to the deformation, the shape and the configuration inside the domain. We present the dependence of these metrics to the radial position of the cell as well as correlations between different metrics, and give

comparisons between high and low hematocrit cases. We demonstrate that cells with a given deformation can acquire different shapes, depending on their position within the domain. Finally, we emphasize the importance of the hematocrit in the studies of cell suspensions, as an increase in the hematocrit causes major alterations in the shape that the cells retain. Therefore, the hematocrit should not be overlooked when designing or optimizing microfluidic devices, but taken into account for the development of highly efficient multi-functional devices, targeted to a larger spectrum of applications and patients.

Future directions of investigation should be focused on investigating deviation of the erythrocyte microstructure from healthy values, to represent changes seen in RBC-related diseases such as HE, HS, SDC and malaria. These types of studies may lead to fundamental understanding of the underlying mechanisms and causes of blood-related diseases and guide the development of diagnostic and therapeutic devices.

7 ACKNOWLEDGEMENTS

We acknowledge support by the European Research Council (ERC Advanced Grant 341117) and computational resources granted by the Swiss National Supercomputing Center (CSCS) under project ID ‘ch7’. We would also like to thank Lina Kulakova for her advice and help in the creation of Fig. 8.

8 APPENDIX

The parameter values used in this work are given in Table 2.

REFERENCES

- [1] M. Abkarian, M. Faivre, and A. Viallat. 2007. Swinging of red blood cells under shear flow. *Physical Review Letters* 98, 18 (2007), 2–5.
- [2] N. Al Quddus, W. A. Moussa, and S. Bhattacharjee. 2008. Motion of a spherical particle in a cylindrical channel using arbitrary Lagrangian–Eulerian method. *J. Colloid Interface Sci.* 317, 2 (2008), 620–630.
- [3] A. M. Altenhoff, J. H. Walther, and P. Koumoutsakos. 2007. A stochastic boundary forcing for dissipative particle dynamics. *J. Comput. Phys.* 225, 1 (2007), 1125–1136.
- [4] J. A. Anderson, C. D. Lorenz, and A. Travesset. 2008. General purpose molecular dynamics simulations fully implemented on graphics processing units. *J. Comput. Phys.* 227, 10 (2008), 5342–5359.
- [5] M. Arienti, W. Pan, X. Li, and G. Karniadakis. 2011. Many-body dissipative particle dynamics simulation of liquid/vapor and liquid/solid interactions. *Journal of Chemical Physics* 134, 20 (2011).
- [6] G. Bao and S. Suresh. 2003. Cell and molecular mechanics of biological materials. *Nat Mater* 2, 11 (2003), 715–725.
- [7] P. S. Becker and S. E. Lux. 1985. Hereditary spherocytosis and related disorders. *Clinics in haematology* 14, 1 (1985), 15–43.
- [8] M. Bernaschi, M. Bisson, M. Fatica, S. Melchionna, and S. Succi. 2013. Petaflop hydrokinetic simulations of complex flows on massive GPU clusters. *Comput. Phys. Comm.* 184, 2 (2013), 329–341.
- [9] E. C. Bingham and R. R. Roepke. 1944. The rheology of blood: IV. The fluidity of whole blood at 37 °C. *The Journal of General Physiology* (1944).
- [10] P. M. Bungay and H. Brenner. 1973. The motion of a closely-fitting sphere in a fluid-filled tube. *Int. J. Multiph. Flow* 1, 1 (1973), 25–56.
- [11] R. C. Cabot, R. E. Scully, E. J. Mark, W. F. McNeely, B. U. McNeely, C. D. Jordan, J. G. Flood, M. Laposata, and K. B. Lewandrowski. 1992. Normal Reference Laboratory Values. *New England Journal of Medicine* 327, 10 (Sept. 1992), 718–724.
- [12] H.-Y. Chang, X. Li, H. Li, and G. E. Karniadakis. 2016. MD/DPD Multiscale Framework for Predicting Morphology and Stresses of Red Blood Cells in Health and Disease. *PLOS Computational Biology* (2016), 1–25.
- [13] S. Chen and G. D. Doolen. 1998. Lattice Boltzmann Method for Fluid Flows. *Ann. Rev. Fluid Mech.* 30 (1998), 329–364.
- [14] S. Chien. 1970. Shear dependence of effective cell volume as a determinant of blood viscosity. *Science* 168, 3934 (1970), 977–979.
- [15] R. Cortez, L. Fauci, and A. Medovikov. 2005. The method of regularized Stokeslets in three dimensions: Analysis, validation, and application to helical swimming. *Physics of Fluids* 17, 3 (2005).
- [16] V. Doyeux, T. Podgorski, S. Peponas, M. Ismail, and G. Couvier. 2011. Spheres in the vicinity of a bifurcation: elucidating the Zweifach–Fung effect. *J. Fluid. Mech.* 674 (2011), 359–388.
- [17] S. Eber and S. E. Lux. 2004. Hereditary spherocytosis defects in proteins that connect the membrane skeleton to the lipid bilayer. In *Seminars in hematology*, Vol. 41. Elsevier, 118–141.
- [18] P. Español. 1995. Hydrodynamics from dissipative particle dynamics. *Physical Review E* 52, 2 (1995), 1734–1742.
- [19] B. Fagrell, M. Intaglietta, and J. Östergren. 1980. Relative hematocrit in human skin capillaries and its relation to capillary blood flow velocity. *Microvascular Research* 20, 3 (Nov. 1980), 327–335.
- [20] R. Fähræus and T. Lindqvist. 1930. The viscosity of the blood in narrow capillary tubes. *American Journal of Physiology–Legacy Content* 96, 3 (1930), 562–568.
- [21] D. A. Fedosov. 2010. *Multiscale modeling of blood flow and soft matter*. Ph.D. Dissertation. Brown University.
- [22] D. A. Fedosov, B. Caswell, and G. E. Karniadakis. 2010. A Multiscale Red Blood Cell Model with Accurate Mechanics, Rheology, and Dynamics SI. *Biophysical Journal* 98, 10 (2010).
- [23] D. A. Fedosov, B. Caswell, A. S. Popel, and G. E. Karniadakis. 2012. Blood Flow and Cell-Free Layer in Microvessels. *Microcirculation* 17, 8 (2012), 615–628.
- [24] D. A. Fedosov, W. Pan, B. Caswell, G. Gompper, and G. E. Karniadakis. 2011. Predicting human blood viscosity in silico. *Phas* 108, 29 (2011), 7–9.

Table 2: Simulation parameter values. L , M and T represent the length, mass and time DPD simulation units respectively. Subscripts ss , sm and mm are for solvent-solvent, solvent-membrane and membrane-membrane DPD interactions.

Parameter	Value	Units
DPD Parameters		
n_d	10	$1/L^3$
Δt	0.0005	T
$k_B T$	0.0444302	ML^2/T^2
γ_{ss}, γ_{mm}	8	M/T
γ_{sm}	10	M/T
a_{ss}, a_{mm}, a_{sm}	2.66667	ML/T^2
m_s	1	M
k	0.25	–
RBC Parameters		
l_0	0.537	L
l_m	1.193	L
p	0.0039	L
k_b	8.091095	ML^2/T^2
k_a	4900	M/T^2
k_d	100	M/T^2
k_v	5000	$M/(LT^2)$
A_{tot}^0	124	L^2
V_0^{tot}	90	L^3
θ_0	6.97°	–
N_t	992	–
N_v	498	–
m_m	0.5	M
LJ Parameters		
σ_{LJ}	0.3	L
ϵ_{LJ}	0.44	ML^2/T^2
Taylor-Couette flow Parameters		
R_{in}	32.73	L
R_{out}	87.27	L
L_{axial}	32	L
Ω_{out}	0.01	$1/T$

- [25] D. A. Fedosov, I. V. Pivkin, and G. E. Karniadakis. 2008. Velocity limit in DPD simulations of wall-bounded flows. *J. Comput. Phys.* 227 (2008), 2540–2559.
- [26] J. B. Freund. 2014. Numerical Simulation of Flowing Blood Cells. *Annual Review of Fluid Mechanics* 46, 1 (2014), 67–95.
- [27] Y.-C. Fung. 1997. *Biomechanics: Circulation*. 571 pages.
- [28] G. Ghigliotti, A. Rahimian, G. Biros, and C. Misbah. 2011. Vesicle migration and spatial organization driven by flow line curvature. *Physical Review Letters* 106, 2 (2011), 1–4.
- [29] P. J. Gilinson, C. R. Dauwalter, and E. W. Merrill. 1963. Viscometer Using an A. C. Torque to Balance Loop and Air Bearing. *Transactions of the Society of Rheology* 7 (1963), 319–331.
- [30] F. K. Glenister, R. L. Coppel, A. F. Cowman, N. Mohandas, and B. M. Cooke. 2002. Contribution of parasite proteins to altered mechanical properties of malaria-infected red blood cells. *Blood* 99, 3 (2002), 1060–1063.
- [31] F. K. Glenister, K. M. Fernandez, L. M. Kats, E. Hanssen, N. Mohandas, R. L. Coppel, and B. M. Cooke. 2009. Functional alteration of red blood cells by a megadalton protein of Plasmodium falciparum. *Blood* 113, 4 (2009), 919–928.
- [32] R. D. Groot and P. B. Warren. 1997. Dissipative particle dynamics: Bridging the gap between atomistic and mesoscopic simulation. *The Journal of Chemical Physics* 107, 11 (1997), 4423.
- [33] P. E. Hadjidakoukas, P. Angelikopoulos, C. Papadimitriou, and P. Koumoutsakos. 2015. Pi4U: A high performance computing framework for Bayesian uncertainty quantification of complex models. *J. Comput. Phys.* 284 (2015), 1–21.
- [34] R. P. Hebbel, N. Mohandas, S. H. Embury, R. P. Hebbel, N. Mohandas, and M. H. Steinberg. 1994. Sickle cell adherence. *Sickle cell disease: basic principles and clinical practice* (1994), 217–230.
- [35] R. P. Hebbel, O. Yamada, C. F. Moldow, H. S. Jacob, J. G. White, and J. W. Eaton. 1980. Abnormal adherence of sickle erythrocytes to cultured vascular endothelium: possible mechanism for microvascular occlusion in sickle cell disease. *Journal of Clinical Investigation* 65, 1 (1980), 154.
- [36] E. Henry, S. H. Holm, Z. Zhang, J. P. Beech, J. O. Tegenfeldt, D. A. Fedosov, and G. Gompper. 2016. Sorting cells by their dynamical properties. *Scientific Reports* 6, October (2016), 34375.
- [37] J. M. Higgins, D. T. Eddington, S. N. Bhatia, and L. Mahadevan. 2007. Sickle cell vasoocclusion and rescue in a microfluidic device. *Proc. Natl. Acad. Sci. U.S.A.* 104, 51 (Dec. 2007), 20496–20500.
- [38] P. J. Hoogerbrugge and J. M. V. A. Koelman. 1992. Simulating Microscopic Hydrodynamic Phenomena with Dissipative Particle Dynamics. *Europhysics Letters (EPL)* 19, 3 (1992), 155–160.
- [39] J. M. Irish, D. K. Czerwinski, G. P. Nolan, and R. Levy. 2006. Altered B-cell receptor signaling kinetics distinguish human follicular lymphoma B cells from tumor-infiltrating nonmalignant B cells. *Blood* 108, 9 (2006), 3135–3142.
- [40] D. Jin, B. Deng, J. X. Li, W. Cai, L. Tu, J. Chen, Q. Wu, and W. H. Wang. 2015. A microfluidic device enabling high-efficiency single cell trapping. *Biomicrofluid.* 9, 1 (2015).
- [41] G. Kabacaoglu, B. Quaife, and G. Biros. 2016. Quantification of mixing in vesicle suspensions using numerical simulations in two dimensions. (2016).
- [42] G. Kabacaoglu, B. Quaife, and G. Biros. 2017. Low-resolution simulations of vesicle suspensions in 2D. (2017).
- [43] N. M. Karabacak, P. S. Spuhler, F. Fachin, E. J. Lim, V. Pai, E. Ozkumur, J. M. Martel, N. Kojic, K. Smith, P.-I. Chen, J. Yang, H. Hwang, B. Morgan, J. Trautwein, T. A. Barber, S. L. Stott, S. Maheswaran, R. Kapur, D. A. Haber, and M. Toner. 2014. Microfluidic, marker-free isolation of circulating tumor cells from blood samples. *Nature Protocols* 9, 3 (2014), 694–710.
- [44] G. Karniadakis and S. Sherwin. 2013. *Spectral/hp element methods for computational fluid dynamics*. Oxford University Press.
- [45] P. Koumoutsakos, I. Pivkin, and F. Milde. 2013. The Fluid Mechanics of Cancer and Its Therapy. *Annual Review of Fluid Mechanics* 45, 1 (2013), 325–355.
- [46] L. D. Landau and E. M. Lifshits. 1959. *Fluid mechanics*. Pergamon Press.
- [47] L. Lanotte, J. Mauer, S. Mendez, D. A. Fedosov, J.-M. Fromental, V. Claveria, F. Nicoud, G. Gompper, and M. Abkarian. 2016. Red cells' dynamic morphologies govern blood shear thinning under microcirculatory flow conditions. *Proc. Natl. Acad. Sci. USA* 113, 47 (Nov. 2016), 13289–13294.
- [48] H. Lei, D. A. Fedosov, B. Caswell, and G. E. Karniadakis. 2013. Blood flow in small tubes: quantifying the transition to the non-continuum regime. *Journal of fluid mechanics* 722, 2013 (2013), 214–239.
- [49] J. Li, M. Dao, C. T. Lim, and S. Suresh. 2005. Spectrin-level modeling of the cytoskeleton and optical tweezers stretching of the erythrocyte. *Biophysical journal* 88, 5 (2005), 3707–19.
- [50] X. Li, A. S. Popel, and G. E. Karniadakis. 2013. Blood-plasma separation in Y-shaped bifurcating microfluidic channels: A dissipative particle dynamics simulation study. *Phys. Biol.* 9, 2 (2013).
- [51] Z. Li and E. E. Dormidontova. 2011. Equilibrium chain exchange kinetics in block copolymer micelle solutions by dissipative particle dynamics simulations. *Soft Matter* 7, 9 (2011), 4179.
- [52] J. L. McWhirter, H. Noguchi, and G. Gompper. 2009. Flow-induced clustering and alignment of vesicles and red blood cells in microcapillaries. *Proceedings of the National Academy of Sciences of the United States of America* 106, 15 (2009), 6039–6043.
- [53] J. L. McWhirter, H. Noguchi, and G. Gompper. 2011. Deformation and clustering of red blood cells in microcapillary flows. *Soft Matter* 7, 22 (2011), 10967.
- [54] E. W. Merrill, E. R. Gilliland, G. Cokelet, H. Shin, A. Britten, and R. E. Wells. 1963. Rheology of Human Blood, near and at Zero Flow: Effects of Temperature and Hematocrit Level. *Biophysical Journal* 3, 3 (1963), 199–213.
- [55] J. P. Mills, M. Diez-Silva, D. J. Quinn, M. Dao, M. J. Lang, K. S. W. Tan, C. T. Lim, G. Milon, P. H. David, O. Mercereau-Puijalon, and others. 2007. Effect of plasmoidal RESA protein on deformability of human red blood cells harboring Plasmodium falciparum. *Proceedings of the National Academy of Sciences* 104, 22 (2007), 9213–9217.
- [56] L. Mountrakis, E. Lorenz, and A. G. Hoekstra. 2013. Where do the platelets go? A simulation study of fully resolved blood flow through aneurysmal vessels. *Interface Focus* 3, 2 (April 2013).
- [57] K. Mueller, D. A. Fedosov, and G. Gompper. 2014. Margination of micro- and nano-particles in blood flow and its effect on drug delivery. *Scientific reports* 4, 4871 (2014), 1–8.
- [58] L. Nan, Z. Jiang, and X. Wei. 2014. Emerging microfluidic devices for cell lysis: a review. *Lab Chip* 14, 6 (2014), 1060–1073.
- [59] D. Pinho, T. Yaginuma, and R. Lima. 2013. A microfluidic device for partial cell separation and deformability assessment. *Biochip J.* 7 (2013), 367–374.
- [60] I. V. Pivkin and G. E. Karniadakis. 2005. A new method to impose no-slip boundary conditions in dissipative particle dynamics. *J. Comput. Phys.* 207, 1 (2005), 114–128.
- [61] I. V. Pivkin and G. E. Karniadakis. 2006. Controlling density fluctuations in wall-bounded dissipative particle dynamics systems. *Physical Review Letters* 96, 20 (2006), 1–4.
- [62] I. V. Pivkin and G. E. Karniadakis. 2008. Accurate Coarse-Grained Modeling of Red Blood Cells. *Physical Review Letters* 101, 11 (2008), 118105.
- [63] S. Plimpton. 1995. Fast Parallel Algorithms for Short-Range Molecular Dynamics. *J. Comput. Phys.* 117, 1 (1995), 1–19.
- [64] B. Quaife and G. Biros. 2014. High-volume fraction simulations of two-dimensional vesicle suspensions. *J. Comput. Phys.* 274 (2014), 245–267.
- [65] D. J. Quinn, I. Pivkin, S. Y. Wong, K. H. Chiam, M. Dao, G. E. Karniadakis, and S. Suresh. 2011. Combined simulation and experimental study of large deformation of red blood cells in microfluidic systems. *Ann. Biomed. Eng.* 39, 3 (2011), 1041–1050.
- [66] A. Rahimian, I. Lashuk, S. K. Veerapaneni, A. Chandramowlishwaran, D. Malhotra, L. Moon, R. Sampath, A. Shringarpure, J. Vetter, R. Vuduc, D. Zorin, and G. Biros. 2010. Petascale direct numerical simulation of blood flow on 200K cores and heterogeneous architectures. *2010 ACM/IEEE Intl. Conf. for High Perf. Computing, Networking, Storage and Analysis, SC 2010* (2010).
- [67] M. Revenga, I. Zuniga, and P. Español. 1999. Boundary conditions in dissipative particle dynamics. *Comput. Phys. Comm.* 121–122, 122 (1999), 309–311.
- [68] D. Rossinelli, Y.-H. Tang, K. Lykov, D. Alexeev, M. Bernaschi, P. Hadjidakoukas, M. Bisson, W. Joubert, C. Conti, G. Karniadakis, M. Fatica, I. Pivkin, and P. Koumoutsakos. 2015. The in-silico lab-on-a-chip: petascale and high-throughput simulations of microfluidics at cell resolution. *Intl. Conf. for High Perf. Computing, Networking, Storage and Analysis (SC'15)* (2015).
- [69] H. Schmid-Schönbein and R. Wells. 1969. Fluid drop-like transition of erythrocytes under shear. *Science (New York, N.Y.)* 165, 3890 (1969), 288–91.
- [70] R. K. Srivastav, Q. S. Ahmed, and A. N. Khan. 2013. Two-phase model of blood flow through a composite stenosis in the presence of a peripheral layer. *J. Multidiscipl. Sci. Res.* 1, 5 (2013), 39–45.
- [71] G. B. Thurston. 1988. Plasma release-cell layering theory for blood flow. *Biorheology* 26, 2 (1988), 199–214.
- [72] R. Tran-Son-Tay, S. P. Sutera, and P. R. Rao. 1984. Determination of red blood cell membrane viscosity from rheoscopic observations of tank-threading motion. *Biophysical Journal* 46 (1984), 65–72.
- [73] D. C. Visser. 2006. Modelling multi-viscosity systems with dissipative particle dynamics. *J. Comput. Phys.* 214, 2 (2006), 491–504.
- [74] D. C. Visser, H. C. J. Hoefsloot, and P. D. Iedema. 2005. Comprehensive boundary method for solid walls in dissipative particle dynamics. *J. Comput. Phys.* 205, 2 (2005), 626–639.
- [75] L. D. Walensky, M. Narla, and S. E. Lux. 2003. Disorders of the red blood cell membrane. *Blood: Principles and Practice of Hematology* (2003), 1709–1858.
- [76] J. C. Way and N. Kleckner. 1985. Transposition of plasmid-borne *Tn10* elements does not exhibit simple length-dependence. *Genetics* 111, 4 (Dec. 1985), 705–713.
- [77] R. Wells and H. Schmid-Schönbein. 1969. Red cell deformation and fluidity of concentrated cell suspensions. *Journal of Applied Rheology* 27, 2 (1969), 213–217.
- [78] S. Wu, P. Angelikopoulos, C. Papadimitriou, R. Moser, and P. Koumoutsakos. 2016. A hierarchical Bayesian framework for force field selection in molecular dynamics simulations. *Phil. Trans. R. Soc. A* 374, 2060 (2016), 20150032.
- [79] S. Yang, A. Ündar, and J. D. Zahn. 2006. A microfluidic device for continuous, real time blood plasma separation. *Lab Chip* 6, 7 (2006), 871–880.

- [80] A. Yazdani and G. E. Karniadakis. 2016. Sub-cellular modeling of platelet transport in blood flow through microchannels with constriction. *Soft Matter* 12 (2016), 4339–4351.
- [81] C. W. Yung, J. Fiering, A. J. Mueller, and D. E. Ingber. 2009. Micromagnetic-microfluidic blood cleansing device. *Lab Chip* 9, 9 (2009), 1171–1177.